



Shape-dependent friction scaling laws in twisted layered material interfaces

Weidong Yan^{a,1}, Xiang Gao^{b,1}, Wengen Ouyang^{a,c,*}, Ze Liu^{a,c,*}, Oded Hod^b, Michael Urbakh^b

^a Department of Engineering Mechanics, School of Civil Engineering, Wuhan University, Wuhan, Hubei 430072, China

^b School of Chemistry and The Sackler Center for Computational Molecular and Materials Science, Tel Aviv University, Tel Aviv 6997801, Israel

^c State Key Laboratory of Water Resources Engineering and Management, Wuhan University, Wuhan, Hubei 430072, China

ARTICLE INFO

Keywords:

Friction scaling law
Layered materials
Twist angle
Moiré superlattice
Interlayer potential
Superlubricity

ABSTRACT

Static friction induced by moiré superstructures in twisted incommensurate finite layered material interfaces reveals unique double periodicity and lack of scaling with contact size. The underlying mechanism involves compensation of incomplete moiré tiles at the rim of rigid polygonal graphene flakes sliding atop fixed graphene or *h*-BN substrates. The scaling of friction (or lack thereof) with contact size is found to strongly depend on the shape of the slider and the relative orientation between its edges and the emerging superstructure, partially rationalizing scattered experimental data. A phenomenological analytical model is developed, which agrees well with detailed atomistic calculations. By carefully considering the edge orientation, twist angle, and sliding direction of the flake relative to the substrate, one should therefore be able to achieve large-scale superlubricity via shape tailoring.

1. Introduction

The scaling up of structural superlubricity, a phenomenon of ultra-low friction and wear emerging in incommensurate layered material junctions, requires the study of the contact size dependence of static and kinetic friction in van der Waals (vdW) interfaces (Berman et al., 2015; Dienwiebel et al., 2004; Hartmuth et al., 2019; Hod et al., 2018; Koren et al., 2016a; Koren et al., 2015; Liu et al., 2012; Mandelli et al., 2018; Qu et al., 2020; Vanossi et al., 2020; Wang et al., 2019a). Previous experimental studies of two-dimensional (2D) contacts suggested various scaling laws of friction with respect to the contact area ($F \propto A^\nu$) with broad scattering of the measured scaling exponent, ranging from 0 (no scaling) to 0.5 (Cihan et al., 2016; Dietzel et al., 2013; Dietzel et al., 2008; Dietzel et al., 2018; Hartmuth et al., 2019; Koren et al., 2015; Özoğul et al., 2017; Wang et al., 2019a). Complementary theoretical and computational studies attributed the observed scattered scaling behavior to the dependence of friction on the shape and relative orientation of the sliding contact (de Wijn, 2012; Müser et al., 2001; Varini et al., 2015), which dictate the specific arrangement of incomplete moiré tiles along the rim of the slider (Koren et al., 2016a; Varini et al., 2015; Wang et al., 2019a; Wang et al., 2019b). Notably, a friction scaling exponent of 0.5 was also found for amorphous 2D contacts (Dietzel et al., 2013; Gnecco et al., 2007; Müser, 2004; Müser et al., 2001), and no scaling was found for triangular gold clusters in contact with hexagonal lattice surfaces (de Wijn,

* Corresponding authors.

E-mail addresses: w.g.ouyang@whu.edu.cn (W. Ouyang), ze.liu@whu.edu.cn (Z. Liu).

¹ These authors contribute equally to this work.

<https://doi.org/10.1016/j.jmps.2024.105555>

Received 28 September 2023; Received in revised form 12 December 2023; Accepted 20 January 2024

Available online 26 January 2024

0022-5096/Â© 2024 Elsevier Ltd. All rights reserved.

2012). Furthermore, different scaling exponents for the sliding energy barrier with contact length have also been predicted for quasi-one-dimensional double-walled nanotubes (DWNTs) depending on the inter-wall lattice commensurability (Damjanović et al., 2002; Kolmogorov et al., 2000; Lozovik et al., 2003).

In this article, we investigate the size dependence of the friction in twisted incommensurate interfaces formed between rigid nanoscale graphene flakes of various shapes and either graphene or *h*-BN rigid substrates. We discover unique double periodicity of the static friction with contact size, induced by moiré superstructures, and lack of size scaling for twisted incommensurate polygonal flakes. Notably, we demonstrate that the frictional scaling strongly depends on the relative orientation between the slider edges and the emerging superstructures.

2. Shape-dependent frictional scaling laws

2.1. Atomistic calculations of static friction in twisted bilayer graphene

Our model systems consist of rigid nanoscale graphene flakes of various shapes (circular, square, triangular, and hexagonal, see Fig. 1a) deposited on a fixed graphene or *h*-BN substrate. The polygonal flakes are cut out of an infinite hexagonal lattice with either armchair or zigzag edges (See Supplemental Material (SM) coordinates file). Interlayer interactions are described by the dedicated anisotropic interlayer potential (ILP) (Leven et al., 2014; Leven et al., 2016b; Maaravi et al., 2017) with refined parameters (Ouyang et al., 2018). To avoid substrate edge effects and spurious interactions between image flakes, periodic boundary conditions are applied in the lateral directions with a sufficiently large supercell, providing a distance larger than 40 Å (more than twice the force-field cutoff of 16 Å) between the flake and its periodic images. The top graphene flakes are initially positioned with their geometric center

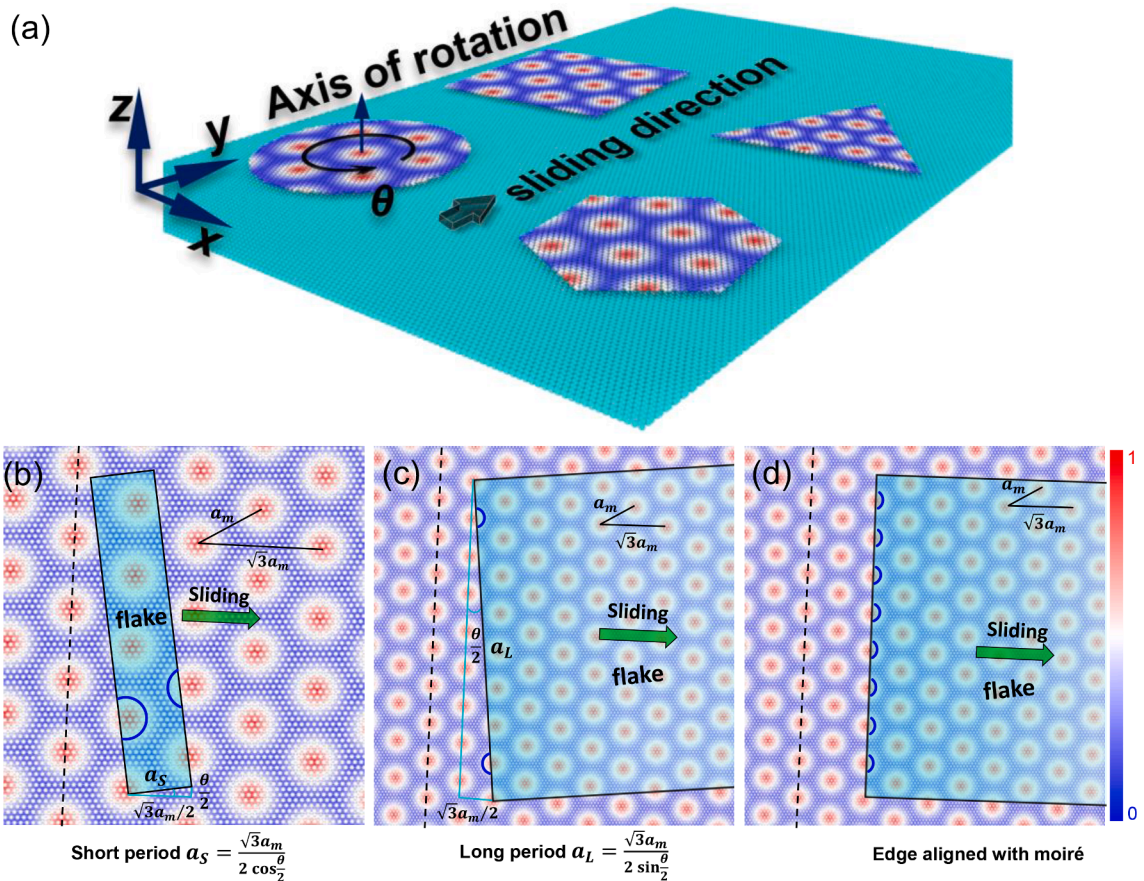


Fig. 1. (a) Model systems of circular, square, triangular, and hexagonal graphene flakes deposited on a fixed graphene substrate with a 5° twist angle. The flakes are rigidly shifted along the armchair direction of the substrate. The color scheme for the flakes (see color bar in panel d), designating the local registry index (LRI) (Cao et al., 2022a; Hod, 2010; Hod, 2012), highlights the moiré superlattices emerging in the twisted interfaces. The cyan colored spheres represent carbon atoms. (b) Illustration of moiré tile compensation at the opposite sides of a rectangular flake (blue circular arcs), occurring when the edge length incorporates approximately an integer number of short moiré periods, a_S . (c) Illustration of moiré tile compensation at the same side of a misaligned rectangular flake (blue circular arcs), occurring when the edge length incorporates approximately an integer number of long moiré periods, a_L . (d) Same as (c) but for the aligned configuration. The black dashed lines in (b)-(d) show one of the moiré superlattice axes.

(appearing at the middle of their central hexagonal ring) above one of the atoms of the underlying graphene or *h*-BN substrate. The flakes are then twisted by an angle θ with respect to the underlying substrate lattice and are rigidly shifted along the armchair direction of the substrate. The interlayer potential energy profile, and the corresponding total resistive force experienced by the flake are recorded along the sliding path. The static friction force for the rigid sliding process is defined as the maximal resistive force experienced by the flake along the sliding path. More calculation details can be found in SM Section 1. We note that for twisted flakes, the sliding direction has no observable effect on the scaling exponent of the static friction with contact size (see SM Section 2).

By neglecting in-plane elastic deformation effects, we are able to isolate the effects of moiré tile incompleteness arising in incommensurate finite contacts of different shapes on the frictional scaling laws. Our simulations show that for the systems considered, the calculated static friction forces obtained for rigid model systems are in good agreement with those obtained for flexible interfaces (see SM Section 3). This is in agreement with previous results demonstrating that the rigid flake assumption reproduces well experimental friction results in supported nanoscale graphitic interfaces, where elasticity effects are suppressed (Hod, 2012). Notably, for the system considered, elasticity effects on the static friction are expected to be significant only at the 10-100 μm length scale (Cao et al., 2022b; Sharp et al., 2016) (see SM Section 3). Hence, our rigid simulation protocol, which is computationally more efficient, allows us to consider large contact area interfaces without compromising the accuracy (Feng et al., 2022).

The color scheme on the surface of the flakes in Fig. 1 designates interlayer lattice registry patterns, obtained via the local registry index (LRI) approach (Cao et al., 2022a; Hod, 2010; Hod, 2012; Leven et al., 2016a), which highlight the moiré superlattices appearing in the twisted interfaces. The period of the moiré superstructures, a_m , is given by (Hermann, 2012; Wang et al., 2019c):

$$a_m = \frac{(1 + \delta)a_{gr}}{\sqrt{2(1 + \delta)(1 - \cos\theta) + \delta^2}}, \quad (1)$$

and its angle with respect to the zigzag direction of the substrate lattice is given by:

$$\psi = \tan^{-1} \left[\frac{(1 + \delta)\sin\theta}{(1 + \delta)\cos\theta - 1} \right] \quad (2)$$

where, $a_{gr} = 2.4602\text{\AA}$ is the period of the hexagonal graphene lattice, θ is the twist angle, and $\delta = a_{sub}/a_{gr} - 1$ is the mismatch between the lattice constants of the interfacing layers (a_{sub} being the lattice constant of the substrate). For the case of a twisted rigid graphitic flake residing on a fixed graphene surface, we have $\delta = 0$, yielding $a_m = \frac{a_{gr}}{2\sin(\theta/2)}$ and $\psi = \frac{\pi}{2} + \frac{\theta}{2}$. Naturally, for a given twist angle, all flake types present the same bulk moiré superstructure, which is expected to be manifested by similar moiré induced frictional characteristics. However, different flake shapes exhibit different incomplete rim moiré tiles along their circumference, which may

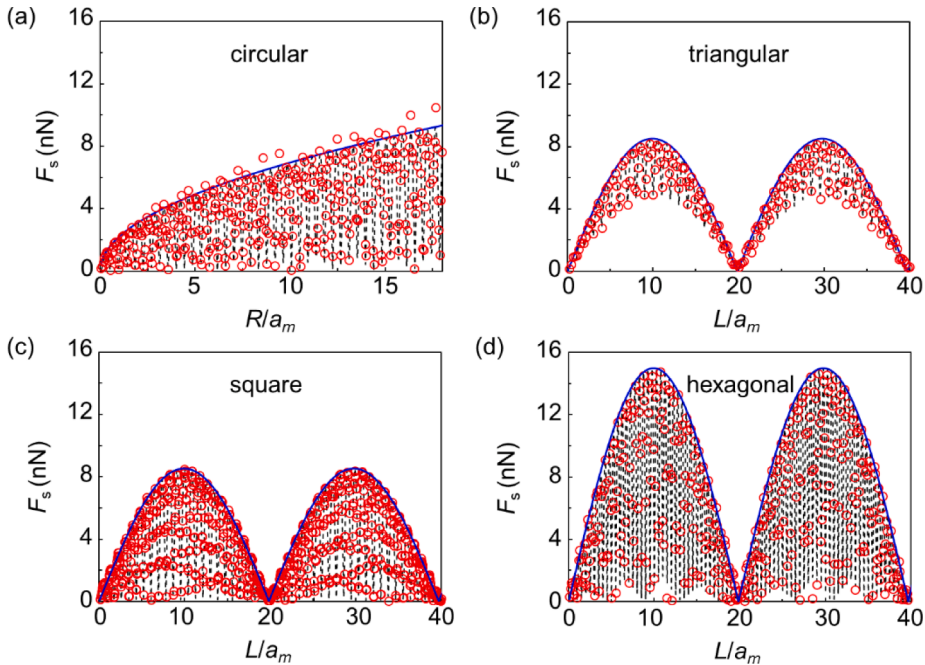


Fig. 2. Size dependence of the static friction of (a) circular, (b) triangular, (c) square, and (d) hexagonal 5° twisted rigid graphene flakes sliding along the armchair direction of a fixed graphene surface. Red circles represent simulation results and black dashed-lines correspond to the theoretical predictions (Eq. (5) in panel (a), Eq. (A.16) in panel (b), Eq. (6) in panel (c), and Eq. (A.20) in panel (d)) obtained using $U_0 = 5.85 \text{ meV/\AA}^2$. The blue solid lines represent the envelopes of friction curves obtained from the theoretical expressions (Eq. (A.15) in panel (a) and Eq. (7) in panels (b)-(d)). R , L and a_m are the radius and side length of the flake and the period of the moiré superlattices, respectively.

induce shape and edge orientation dependent frictional scaling behavior with increasing contact size.

Fig. 2 presents the calculated static friction force as a function of flake size (radius or side length) normalized by the moiré period of incommensurate, 5° twisted, homogeneous graphitic contacts of different shapes. Notably, regardless of the flake shape, the static friction exhibits undulations with a period of the order of moiré supercell dimension, consistent with previous predictions (Gigli et al., 2017; Koren et al., 2016a; Koren et al., 2016b; Wang et al., 2019a; Yaniv et al., 2019). However, the larger scale behavior, dictated by the incomplete rim moiré tiles, shows different scaling with contact size for circular shaped flakes compared to that of the polygonal ones. The friction force scaling behavior obtained for the former (Fig. 2a) matches well previous results (Koren et al., 2016a; Yan et al., 2023), showing an increase with the fourth root of the contact area ($A^{1/4}$). For the polygonal shaped flakes (Fig. 2b-d), on top of the moiré-level friction undulations, the static friction force exhibits an additional periodic behavior on an order of magnitude larger length-scale. Surprisingly, in contrast with the case of the circular shaped flakes, no overall increase of friction with contact area is observed for the polygonal shaped ones. Notably, this finding seems to contradict previous predictions of linear scaling of the friction with side length in hexagonal shaped flakes (Koren et al., 2016a). This linear scaling, however, stems from the fact that in Ref. (Koren et al., 2016a), a twist angle dependent cut was imposed, where the flakes edges were chosen parallel to the moiré superlattice axes (see Appendix A).

2.2. The physical mechanism underlying double-periodic friction modulations

To understand the origin of the double-periodic modulation behavior, we compare the size dependence of the sliding potential energy barrier along the sliding path and the corresponding variations of the global registry index (GRI) (Koren et al., 2016c), a simple geometric measure of interlayer lattice registry (see SM Section 4). The excellent agreement between the two measures indicates that the conditions for vanishing sliding energy barriers and static friction forces have a geometric origin. This can be further quantified by considering local registry index (LRI) (Cao et al., 2022a; Hod, 2010; Hod, 2012) maps (see Fig. 1b-c) that reveal the central role played by the moiré superstructures along the flake sides. Specifically, two different conditions can be fulfilled in order for the static friction to vanish, which are easiest to demonstrate for the case of square flakes. The first condition is the compensation of incomplete moiré tiles on the front and back sides of the sliding flake, which occurs when the distance between these sides is approximately an integer multiple of the moiré period in the direction perpendicular to those sides (see Fig. 1b), $a_s = \frac{\sqrt{3}a_m}{2\cos(\theta/2)}$. This leads to the short periodicity of the static friction force observed in Fig. 2c. The second condition corresponds to the incorporation of approximately an integer number of moiré tiles on either the front or back sides of the square flake, leading to “self-compensation” with a longer period (see Fig. 1c), written as:

$$a_L = \frac{\sqrt{3}a_m}{2\sin(\theta/2)} \quad (3)$$

While similar conditions apply also for other regular polygonal structures, especially those with parallel sides, circular flakes lack straight sides and thus do not exhibit the larger friction oscillation period corresponding to the self-compensation effect.

3. Analytical model

A more quantitative analysis of the discovered double-periodic behavior and size scaling (or lack of) can be obtained via an analytical model that assumes that the interaction between the flake and the substrate is described by a moiré induced periodic potential. Treating the flake as a continuum surface, the potential experienced by an infinitesimal surface area of the flake can be approximated as (Dong et al., 2011; Huang et al., 2022; Steiner et al., 2009; Verhoeven et al., 2004; Yan et al., 2022) (see Appendix A):

$$dU = \pm \frac{2}{9} U_0 \left[2\cos\frac{2\pi x}{\sqrt{3}a_m} \cos\frac{2\pi y}{a_m} + \cos\frac{4\pi x}{\sqrt{3}a_m} \right] dx dy, \quad (4)$$

where U_0 is the amplitude of the potential energy landscape corrugation per unit area, and the plus or minus signs apply for graphene or *h*-BN substrates, respectively. Integrating Eq. (4) over the entire flake area $S_{\text{flake}}(x_0, y_0)$, where (x_0, y_0) is the geometric center of the flake, yields the shape and position dependent interaction energy between the flake and the substrate, $E(x_0, y_0) = \int_{S_{\text{flake}}(x_0, y_0)} dU$.

Considering that the contribution of complete bulk moiré tiles to the total potential variations during sliding vanishes (Yan et al., 2023), the changes in the corresponding integrated interlayer potential energy originate entirely from the incomplete rim moiré tiles. The derivative of the total energy with respect to x_0 (or y_0) gives the resistive force in the armchair (or zigzag) directions, for a given flake displacement, the maximum of which along the sliding path is defined as the static friction force F_s (see SM Section 1).

For circular flakes, this model yields a static friction force of the following form (Cao et al., 2022b; Morovati et al., 2022; Yan et al., 2023) (see Appendix A):

$$F_s^{\text{Circ}}(R) = \frac{\alpha a_m \pi R U_0}{a_{\text{sub}}} \left| J_1 \left(\frac{4\pi R}{\sqrt{3}a_m} \right) \right|, \quad (5)$$

where, $J_1(\cdot)$ is the Bessel function of the first kind, α is a coefficient that depends on the sliding direction ($\alpha \approx 0.7823$ for the scan line chosen in this study, see Eq. (A.14)), and R is the radius of the flake. The dashed line in Fig. 2a presents $F_s^{\text{Circ}}(R)$ calculated according to

Eq. (5), showing excellent agreement with the simulation results (open red circles). In this case, only the short periodicity (of the order of the moiré superstructure dimensions) prevails with an envelope that scales asymptotically as $A^{1/4}$ as expected (see Appendix A).

For the polygonal shaped flakes, somewhat more involved static friction expressions are obtained (see Appendix A and Table 1). For example, for square shaped flakes at small twist angles one gets:

$$F_s^{\text{Sq}}(L, \theta) \approx \left| \frac{2\sqrt{3}a_m^2 U_0}{9\pi a_{\text{sub}} \sin \frac{\theta}{2} \cos \frac{\theta}{2}} \sin \left(\frac{2\pi L \cos \frac{\theta}{2}}{\sqrt{3}a_m} \right) \sin \left(\frac{2\pi L \sin \frac{\theta}{2}}{\sqrt{3}a_m} \right) \right|. \quad (6)$$

Corresponding expressions for triangular and hexagonal flakes are presented in Appendix A and Table 1. For all polygonal shaped flakes considered, excellent agreement is found between the theoretical model results (black dashed lines in Fig. 2) and the simulation results (open red circles). A qualitatively different behavior of the short period oscillations is found for the triangular flake (Fig. 2b), where the absence of parallel sides leads to less efficient cancellation of incomplete moiré superlattices. As a result, there is no full elimination of static friction force in the lower envelope of the short period oscillations. The corresponding oscillation amplitude for the square (Fig. 2c) and hexagonal (Fig. 2d) flakes, with parallel sides, does lead to efficient compensation and vanishing static friction force.

As is evident in Table 1, the model prediction for the asymptotic ($L/a_m \gg 1$) behavior of the envelopes of $F_s(L, \theta)$ for the polygonal flakes reads as follows:

$$F_s^{\text{env}}(L, \theta) \propto \left| \sin \left(\frac{2\pi L \sin \frac{\theta}{2}}{\sqrt{3}a_m} \right) \right|, \quad (7)$$

where L is the side length of the flake. This expression clearly demonstrates that for the polygonal shaped flakes considered, the static friction force does not overall grow with the flake side length. Moreover, they present the same long period of $\frac{\sqrt{3}a_m}{2\sin(\theta/2)}$ (see Fig. 2b-d), reflecting the universal self-compensation of incomplete moiré tiles at the sides with angle of $\theta/2$ to the moiré superlattice directions. We note that when considering friction as a function of contact area, the long modulation periods become shape-dependent. Naturally, this arises from pure geometric considerations relating the side length to the regular polygon area, $L = 2\sqrt{A \cdot \tan(\pi/N)/N}$. Written in terms of the contact area, the long periodicity ($\sqrt{A_l}$) of the static friction grows with increasing side number, N , as $\sqrt{A_l} = \sqrt{\frac{N}{\tan(\pi/N)} \frac{a_c}{2}} \approx \frac{Na_c}{2\sqrt{\pi}}$, thus approaching infinity at the circular flake limit ($N \rightarrow \infty$). This is manifested by the fact that the envelope of the $N = 50$ curve in Fig. S7 of the SM matches the curve of the circular flake. Therefore, a smooth transition of the friction force scaling between polygonal and circular shaped flakes with increasing number of polygon sides is predicted.

4. General nature of the double-periodic modulation and friction scaling with contact size

Furthermore, to verify that our findings are not limited to regular polygonal shaped flakes, we performed additional simulations, accompanied by theoretical model predictions, for irregular shaped flakes (see SM Sec. 6). The results show that the predicted long-period modulation of the static friction and the lack of frictional scaling with system size are robust and expected also for irregular polygonal shaped flakes. Nonetheless, the introduction of curved edges, whose curvature varies with flake size results in frictional scaling with an exponent of $1/4$, reminiscent of the case of circular flakes (see SM Secs. 6 and 8).

The qualitative nature of the double-periodic behavior remains unchanged with increasing twist angle, as long as the moiré superstructure dimensions are substantially larger than the lattice constant and smaller than the side length of the flake. Due to the moiré superlattice size reduction, both periodicities and the friction amplitude decrease with increasing twist angle (see Fig. 3a for square flakes results). As may be expected, the short periodicity, a_s , which is directly related to the moiré superstructure dimensions,

Table 1

Summary of the analytical expressions obtained for the static friction (F_s) and its envelope (F_s^{env}) for different flake shapes at small angles between one polygonal flake side and the moiré superlattice, given by $\theta_1 = \frac{\theta}{2}$ for homogeneous graphene interfaces and $\theta_1 = \psi - \theta$ for heterogeneous graphene/h-BN interfaces.

Flake Shape	F_s	F_s^{env}
Square	$\left \frac{2\sqrt{3}a_m^2 U_0}{9\pi a_{\text{sub}} \sin \theta_1 \cos \theta_1} \sin \left(\frac{2\pi L \cos \theta_1}{\sqrt{3}a_m} \right) \sin \left(\frac{2\pi L \sin \theta_1}{\sqrt{3}a_m} \right) \right $	$\left \frac{2\sqrt{3}a_m^2 U_0}{9\pi a_{\text{sub}} \sin \theta_1 \cos \theta_1} \sin \left(\frac{2\pi L \sin \theta_1}{\sqrt{3}a_m} \right) \right $
Triangular	$\left \frac{2a_m^2 U_0 \cot \theta_1}{\sqrt{3}\pi(1 + 2\cos 2\theta_1)a_{\text{sub}}} \sin \left(\frac{2\pi L \sin \theta_1}{\sqrt{3}a_m} \right) \right $	$\left \frac{2\pi L \sin \theta_1}{\sqrt{3}a_m} \right $
Hexagonal	$\frac{(\sqrt{3} + \sqrt{11})\sqrt{30 + 2\sqrt{33}}a_m^2 U_0}{16\pi(1 + 2\cos 2\theta_1)a_{\text{sub}}} \left \cot \theta_1 \sin \left(\frac{2\pi L \cos \theta_1}{a_m} \right) \sin \left(\frac{2\pi L \sin \theta_1}{\sqrt{3}a_m} \right) \right $	$\frac{(\sqrt{3} + \sqrt{11})\sqrt{30 + 2\sqrt{33}}a_m^2 U_0}{48\pi(1 + 2\cos 2\theta_1)a_{\text{sub}}} \left \cot \theta_1 \sin \left(\frac{2\pi L \sin \theta_1}{\sqrt{3}a_m} \right) \right $
Circular	$\frac{(3 + \sqrt{33})\sqrt{30 + 2\sqrt{33}}}{72} \frac{a_m \pi R U_0}{a_{\text{sub}}} \left J_1 \left(\frac{4\pi R}{\sqrt{3}a_m} \right) \right $	$\frac{3}{24} \frac{1}{a_{\text{sub}}} \frac{(\sqrt{3} + \sqrt{11})\sqrt{5\sqrt{3} + \sqrt{11}}}{a_m^2 R^2 U_0}$

scales as $a_m \propto \sin^{-1}(\frac{\theta}{2})$. As per Eq. (3), the scaling of the long periodicity, a_L , is a_m^2 . The maximal friction force, $F_s^{\max}(\theta)$, can be obtained by taking the maximum of Eq. (6), yielding:

$$F_s^{\max}(\theta) = \frac{4\sqrt{3}a_m^3 U_0}{9\pi a_m^2 \cos^2 \frac{\theta}{2}} = \frac{\sqrt{3}a_{gr} U_0}{18\pi \sin^3 \frac{\theta}{2} \cos^2 \frac{\theta}{2}}, \tag{8}$$

which scales with a_m^3 or $\sin^{-3}(\frac{\theta}{2})$, as shown in Fig. 3b.

The revealed double-periodic frictional behavior and the lack of frictional size-scaling for polygonal structures are not limited to homogeneous graphitic interfaces. To demonstrate this, we repeated our calculations for the heterogeneous interface of graphene and hexagonal boron nitride (*h*-BN). The intrinsic lattice mismatch ($\delta \approx 1.8\%$) of the two materials gives interfacial incommensurability also at the aligned configuration, with a moiré superstructure period of $a_m \approx 13.9$ nm, leading to ultralow friction at any twist angle (Leven et al., 2013; Leven et al., 2016b; Liao et al., 2021; Song et al., 2018). This allows us to study also aligned contacts while avoiding high-friction commensurate states. Fig. 4 compares friction results for aligned and 1° twisted circular and square shaped graphitic flakes sliding along the armchair direction of the underlying rigid *h*-BN substrate. Similar to the case of homogeneous circular interfaces, the circular shaped heterogeneous junctions exhibit periodic oscillations with an envelope scaling of $F_s \propto A^{1/4}$ (matching Eq. (5)) for both the aligned (Fig. 4a) and twisted (Fig. 4b) configurations. The heterogeneous square interfaces exhibit qualitatively different frictional size-scaling for the aligned (Fig. 4c) and twisted (Fig. 4d) configurations. The $\theta = 1^\circ$ twisted system presents double-periodic behavior, similar to that of the homogeneous square interface, with quantitative differences that originates from the large rotation ($\psi = 44.9^\circ$) of the moiré superstructure (see Sec. 7 of SM). The aligned square interface, whose sides are parallel to the moiré superstructure, exhibits only the short-period oscillations with an envelope that scales as $F_s \propto L \propto A^{1/2}$ (see Fig. 4c), reminiscent of previous results (Koren et al., 2016b). This is due to the fact that in this case all incomplete tiles are identical and vary in phase when the flake slides in all directions except the one parallel to this side (see Fig. 1d), such that self-compensation is prohibited. Furthermore, since the number of incomplete moiré tiles grows proportionally to the flake side length, the static friction scales linearly with system dimensions. This unique orientational effect is well captured by the analytical model for square flakes (see Table 1), which demonstrates zero scaling with flake side length for misaligned configurations, whereas for the aligned case ($\theta_1 \rightarrow 0$) it yields:

$$F_{s,\text{sqf}}^{\text{env}}(L) \approx \frac{4a_m U_0 L}{9a_{\text{sub}}}, \tag{9}$$

giving linear scaling with side length. Similar expressions are obtained for other polygonal flakes in the aligned configuration (see, for instance, Eq. (A.22) for hexagonal flakes), demonstrating the general nature of this finding.

We note that the analytical model predicts only double periodicity for the three equilateral polygonal shapes investigated. Nonetheless, additional periodicities may occur for asymmetric polygonal flakes due to the combined effect of different periods associated with the various flake sides. Interestingly, the physical origin of these periodic behaviors is different from that predicted for the interwall sliding barrier of DWNTs, where the long period appears when the transitional vectors of the inner and outer tube walls have a common divisor (or close to having one) (Damjanović et al., 2002; Kolmogorov et al., 2000; Lozovik et al., 2003).

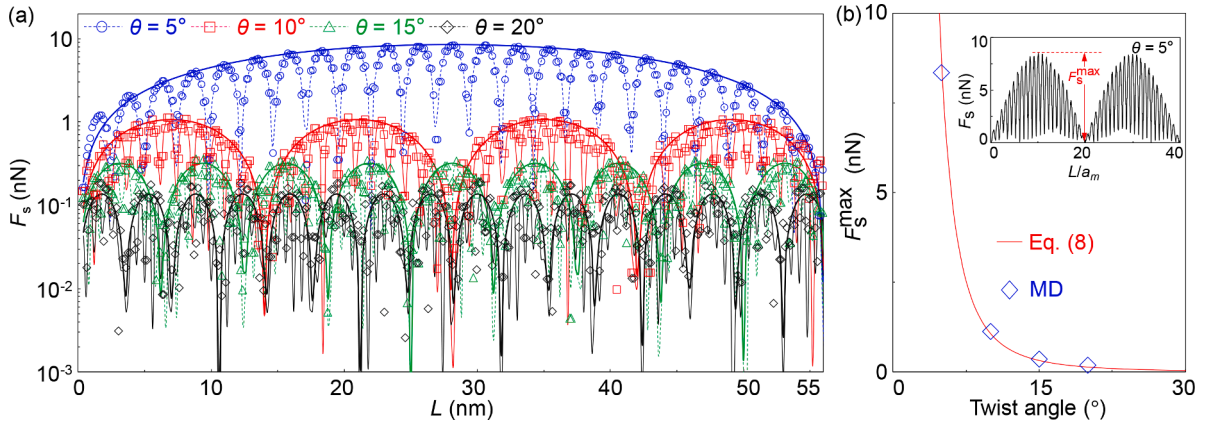


Fig. 3. Size dependence of the static friction of square rigid graphene flakes sliding along the armchair direction of a fixed graphene surface at twist angles of 5° (blue circle), 10° (red square), 15° (green triangular), and 20° (black diamond). Open circles, dashed lines, and solid lines represent results of atomistic calculations, theoretical predictions (Eq. (6)), and the envelope curves (Eq. (7)), respectively, obtained using the same parameters as in Fig. 2. (b) Twist angle-dependence of the maximal static friction for a square rigid graphene flake. The inset illustrates the determination of F_s^{\max} for $\theta = 5^\circ$.

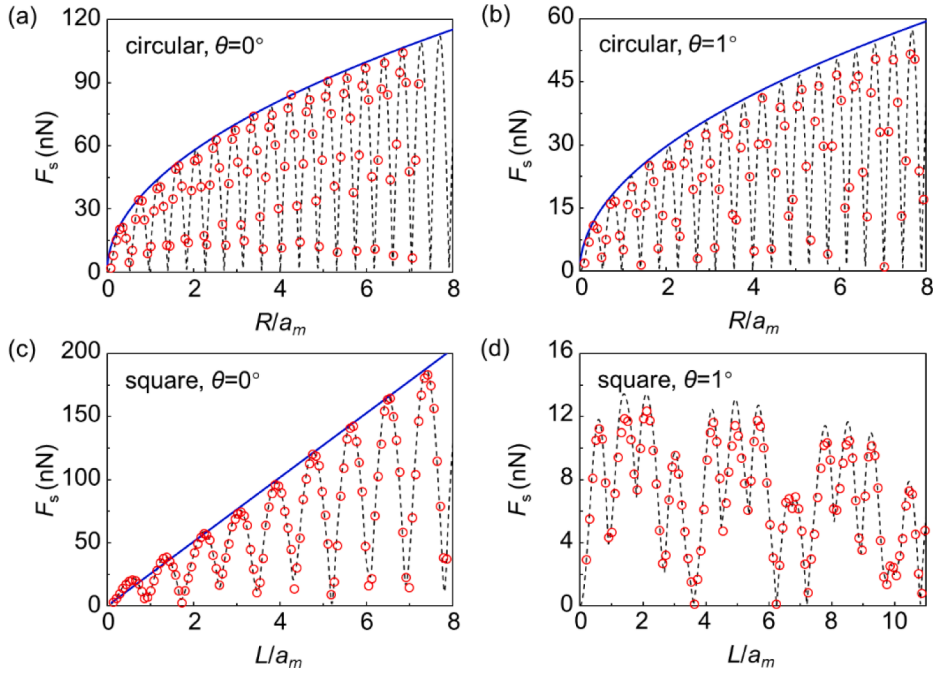


Fig. 4. Size dependence of the static friction of (a, b) circular and (c, d) square graphene flakes sliding in the (a, c) aligned or (b, d) 1° twisted configurations along the armchair direction of an h -BN substrate. Red circles represent simulation results and black dashed-lines correspond to the theoretical model predictions (Eq. (5) in panels (a)-(b), Eq. (A.11) in panel (c), and Eq. (A.7) in panel (d)) obtained using $U_0 = 4.5 \text{ meV}/\text{\AA}^2$. The blue solid lines represent the envelopes of the friction curves obtained from the theoretical expressions (Eq. (A.15) in panels (a) and (b), and Eq. (9) in panel (c)). R , L and a_m are the circle radius, side length of the square flake, and the period of the moiré superlattices, respectively. The latter being $a_m = 13.9 \text{ nm}$ and $a_m = 9.9 \text{ nm}$ for $\theta = 0^\circ$ and 1° , respectively.

5. Conclusions

To put our results into context, we note that existing experimental measurements suggested a power law scaling of the friction (mainly kinetic) with contact area, $F_k \propto A^\gamma$, but with relatively wide scatter of the reported data (Cihan et al., 2016; Dietzel et al., 2017; Dietzel et al., 2013; Dietzel et al., 2008; Hartmuth et al., 2019; Koren et al., 2016a; Koren et al., 2016b; Koren et al., 2015; Liao et al., 2021; Qu et al., 2020; Varini et al., 2015; Wang et al., 2019a). Theoretical studies further attributed different values of γ to the shape of the sliding nanoflakes and its relative orientation with respect to the underlying layered material substrates (de Wijn, 2012; Dietzel et al., 2013; Varini et al., 2015). Our results show that static friction scaling with contact area in layered interfaces strongly depends on the shape of the slider and the specific orientation in which it is cut with respect to the emerging interfacial moiré superstructures. This may lead to various scaling behaviors with $\gamma = 0$ for twisted polygonal flakes with edges that do not coincide with the moiré superlattice, 0.25 for circular shaped flakes, and 0.5 when the edges of polygonal flakes are parallel to the moiré superstructure. Since the static friction force scaling with contact dimensions obtained in our rigid flake calculations is in good agreement with that obtained for flexible interfaces (see SM Section 3) and since the latter serves as an upper limit for the corresponding kinetic friction of these systems, we expect strong dependence of the kinetic friction scaling on these factors, as well. This, in turn, may partially rationalize the wide scattering of results observed in experiments measuring the size dependence of friction. Other factors including edge chemical contamination, poor control over the twist angle (Feng et al., 2013; Filippov et al., 2008; Qu et al., 2020) (see also Appendix A), as well as elastic effects (Sharp et al., 2016) may further contribute to the experimentally observed data scattering. Therefore, when setting to explore the size dependence of friction in layered interfaces, one should carefully consider the shape of the studied contacts, their orientation, twist angle, and sliding direction. This should allow for unveiling the predicted novel tribological phenomena including multiple-periodicities and lack of size scaling, thus opening the way for obtaining large-scale superlubricity via shape tailoring.

CRedit authorship contribution statement

Weidong Yan: Conceptualization, Data curation, Formal analysis, Validation, Visualization, Writing – original draft, Writing – review & editing. **Xiang Gao:** Conceptualization, Data curation, Visualization, Writing – original draft, Writing – review & editing, Formal analysis, Validation. **Wengen Ouyang:** Conceptualization, Funding acquisition, Investigation, Methodology, Writing – review & editing. **Ze Liu:** Conceptualization, Funding acquisition, Investigation, Methodology, Writing – review & editing. **Oded Hod:** Conceptualization, Funding acquisition, Investigation, Methodology, Writing – review & editing. **Michael Urbakh:** Conceptualization, Funding acquisition, Investigation, Methodology, Writing – review & editing.

Declaration of competing interest

The authors declare that they have no known competing financial interests or personal relationships that could have appeared to influence the work reported in this paper.

Data availability

Data will be made available on request.

Acknowledgements

W. O., and Z. L. would like to acknowledge supports from the National Natural Science Foundation of China (Nos. 12102307, 12172260 and 11890673), the Key Research and Development Program of Hubei Province (2021BAA192), the Fundamental Research Funds for the Central Universities (Nos. 2042023kf0233 and 2042022kf1177) and the starting-up fund of Wuhan University. W. Y. would like to acknowledge supports from the China Postdoctoral Science Foundation (No. GZC20231978). X. G. acknowledges the postdoctoral fellowships of the Sackler Center for Computational Molecular and Materials Science and the Ratner Center for Single Molecule Science at Tel Aviv University. M. U. acknowledges the financial support of the Israel Science Foundation, Grant No. 1141/18 and the ISF-NSFC joint Grant No. 3191/19. O. H. is grateful for the generous financial support of the Israel Science Foundation under Grant No. 1586/17, the Heineman Chair in Physical Chemistry, Tel Aviv University Center for Nanoscience and Nanotechnology, and the Naomi Foundation for generous financial support via the 2017 Kadar Award. Computations were conducted at the National Supercomputer TianHe-1(A) Center in Tianjin and the Supercomputing Center of Wuhan University.

Supplementary materials

Supplementary material associated with this article can be found, in the online version, at [doi:10.1016/j.jmps.2024.105555](https://doi.org/10.1016/j.jmps.2024.105555).

Appendix A. Analytical approach for calculating the static friction force

In this appendix, we introduce a detailed theoretical approach for calculating the static friction force of twisted layered interfaces at which moiré superlattices form. For incommensurate hexagonal layered material interfaces, such as twisted bilayer graphene or graphene/h-BN, one can construct a continuum interlayer potential with the following potential energy density function (Dong et al., 2011; Huang et al., 2022; Steiner et al., 2009; Verhoeven et al., 2004; Yan et al., 2022):

$$U(x, y) = \pm \frac{2}{9} U_0 \left[2 \cos\left(\frac{2\pi x}{\sqrt{3}a_m}\right) \cos\left(\frac{2\pi y}{a_m}\right) + \cos\left(\frac{4\pi x}{\sqrt{3}a_m}\right) \right], \quad (\text{A.1})$$

where the y -axis resides along one of the moiré superlattice vector, U_0 is the potential energy density corrugation, a_m is the moiré superlattice period, and the \pm sign applies for twisted bilayer graphene and graphene/h-BN interfaces, respectively. Fig. A1 compares the pair-averaged interlayer potential energy density calculated using the dedicated ILP (Leven et al., 2014; Leven et al., 2016b; Maaravi et al., 2017; Ouyang et al., 2018) with a refined parameterization (Ouyang et al., 2018) for (a) 5° twisted bilayer graphene and (c) aligned graphene/h-BN, with the corresponding continuum model potential energy density of Eq. (A.1) (b, d). Clearly, the continuum model potential energy, which enables us to extract analytic expressions for the static friction force, has the appropriate symmetry of the atomic potential and captures well the potential energy corrugation – two characteristics that are important for the static friction calculations. The somewhat smoothed hexagonal structure of the continuum model potential energy is found to have a minor effect on the qualitative conclusions of our analytic expressions.

Using the approximated continuum model potential energy density function of Eq. (A.1), we can derive analytic expressions for the static friction force experienced by flakes of different shapes that allow for deciphering the origin of the double-periodic behavior with contact size discussed in the main text, as well as the asymptotic scaling.

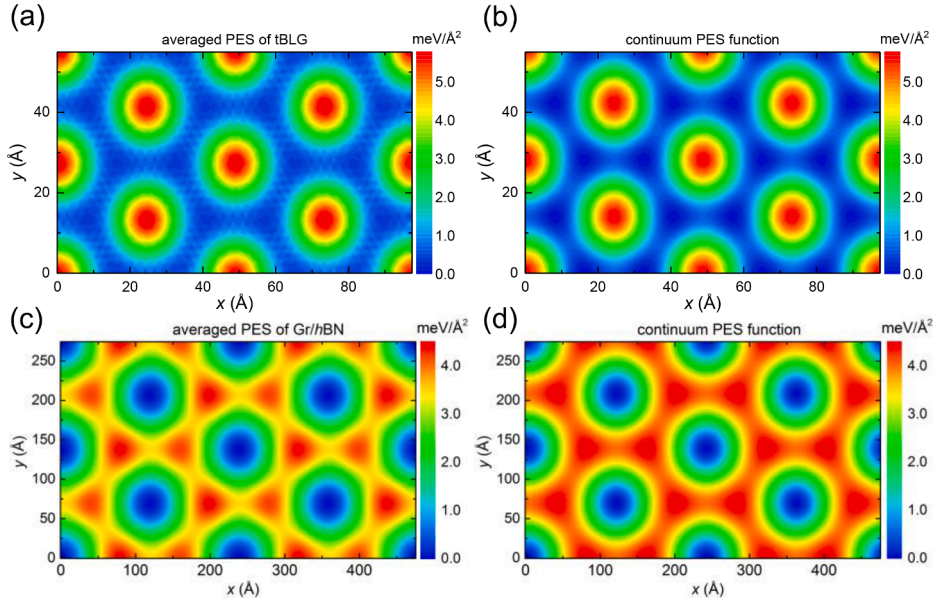


Fig. A1. Comparison between the pair-averaged interlayer potential energy density map of a (a) 5° twisted bilayer graphene interface and (c) aligned graphene/h-BN bilayer, and (b, d) the corresponding continuum model potential energy density maps (Eq. (A.1)). To avoid atomic scale sharp features, the pair-averaged atomic potential energy is calculated by averaging the potential energy of each covalently bonded carbon pair in the flake interacting with the substrate, and assigning the average value, normalized by the area occupied by a single atom (2.62 \AA^2), to the center of the bond formed by the carbon pair. In panels (b) and (d) U_0 is 5.85 and 4.5 meV/Å², respectively.

To obtain analytical expressions for the static friction force, one has to integrate the potential energy density expression over the entire flake area. The result of this integration will depend on the shape, size, and twist angle of the flake, as well as on the identity of the substrate. Given a general twist angle, θ , between the contacting surfaces (defined here as the angle between the zigzag directions of the interfacing hexagonal lattices), the moiré superlattice period is given by Eq. (1) (Hermann, 2012; Wang et al., 2019c). For the description of the static friction, it is convenient to introduce the angle θ_1 between one of the sides of a polygonal shaped flake and the moiré superlattice. Since in the present study all polygonal flakes are cut with either armchair or zigzag edges, we have $\theta_1 = \frac{\theta}{2}$ for homogeneous graphene interfaces and $\theta_1 = \psi - \theta$ for heterogeneous graphene/h-BN interfaces, where ψ is defined in Eq. (2). For the purpose of the integration, one further needs the following transformation that relates between the coordinate system of the flake (x', y'), where x' is aligned with the zigzag (armchair) direction of the hexagonal lattice of the graphene flake in the homogeneous (heterogeneous) junction, and that of the moiré superlattice (x, y):

$$\begin{cases} x = x' \cos \theta_1 + y' \sin \theta_1 \\ y = -x' \sin \theta_1 + y' \cos \theta_1 \end{cases} \quad (\text{A.2})$$

The two reference frames are taken to have a common origin located at a potential maximum (minimum) for homogeneous graphene (heterogeneous graphene/h-BN) interfaces. Note that the origin is not necessarily located within the flake.

The various angles defined above, as well as the two reference frames, are illustrated in Fig. A2 for the $\theta = 5^\circ$ homogeneous graphene interface and in Fig. S10 for the $\theta = 1^\circ$ heterogeneous graphene/h-BN interface.

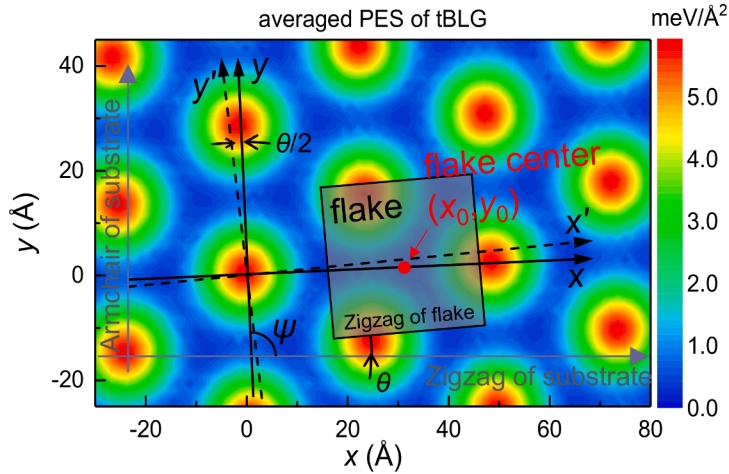


Fig. A2. Illustration of the moiré (x, y) and flake (x', y') reference frames plotted atop the pair-averaged potential energy density map of a $\theta = 5^\circ$ twisted square graphene flake sliding atop a graphene surface. The reference frames are rotated with respect to each other by an angle of $\theta/2 = 2.5^\circ$.

A.1. Square flakes

For a square flake of side-length L , the integration of the potential energy density at a given flake position is performed as follows:

$$E_{\text{sqr}}(x'_0, y'_0, L, \theta_1) = \int_{x'_0 - \frac{L}{2}}^{x'_0 + \frac{L}{2}} \int_{y'_0 - \frac{L}{2}}^{y'_0 + \frac{L}{2}} U(x', y', \theta_1) dx' dy', \quad (\text{A.3})$$

Here, (x'_0, y'_0) is the position of the geometric center of the flake, written in the reference frame of the flake. Note that for simplicity the integration is performed in the reference frame of the twisted flake, whereas Eq. (A.1) is written in the moiré superlattice reference frame. Hence, the arguments of the potential in Eq. (A.3) include the angle between the two reference frames. Substituting Eqs. (A.1) and (A.2) into (A.3) yields:

$$E_{\text{sqr}}(x'_0, y'_0, L, \theta_1) = \pm \frac{2}{9} U_0 \int_{x'_0 - \frac{L}{2}}^{x'_0 + \frac{L}{2}} \int_{y'_0 - \frac{L}{2}}^{y'_0 + \frac{L}{2}} \left[2 \cos \frac{2\pi(x' \cos \theta_1 + y' \sin \theta_1)}{\sqrt{3}a_m} \cos \frac{2\pi(-x' \sin \theta_1 + y' \cos \theta_1)}{a_m} + \cos \frac{4\pi(x' \cos \theta_1 + y' \sin \theta_1)}{\sqrt{3}a_m} \right] dx' dy', \quad (\text{A.4})$$

which can be written explicitly as:

$$E_{\text{sqr}}(x'_0, y'_0, L, \theta_1) = \frac{\mp 4a_m^2 U_0}{\pi^2(1 + 2\cos 4\theta_1)} \left[\csc 2\theta_1 \sin\left(\frac{\pi}{3} - 2\theta_1\right) \sin\left(\frac{\pi}{3} + 2\theta_1\right) \sin\left(\frac{2\pi L \cos \theta_1}{\sqrt{3}a_m}\right) \sin\left(\frac{2\pi L \sin \theta_1}{\sqrt{3}a_m}\right) \cos\left(\frac{4\pi(x'_0 \cos \theta_1 + y'_0 \sin \theta_1)}{\sqrt{3}a_m}\right) \right. \\ \left. + \sin\left(\frac{\pi}{3} - 2\theta_1\right) \cos\left(\frac{4\pi(x'_0 \cos(\frac{\pi}{3} - \theta_1) - y'_0 \sin(\frac{\pi}{3} - \theta_1))}{\sqrt{3}a_m}\right) \sin\left(\frac{2\pi L \cos(\frac{\pi}{3} - \theta_1)}{\sqrt{3}a_m}\right) \sin\left(\frac{2\pi L \sin(\frac{\pi}{3} - \theta_1)}{\sqrt{3}a_m}\right) \right. \\ \left. + \sin\left(\frac{\pi}{3} + 2\theta_1\right) \cos\left(\frac{4\pi(x'_0 \cos(\frac{\pi}{3} + \theta_1) + y'_0 \sin(\frac{\pi}{3} + \theta_1))}{\sqrt{3}a_m}\right) \sin\left(\frac{2\pi L \cos(\frac{\pi}{3} + \theta_1)}{\sqrt{3}a_m}\right) \sin\left(\frac{2\pi L \sin(\frac{\pi}{3} + \theta_1)}{\sqrt{3}a_m}\right) \right]. \quad (\text{A.5})$$

In the results presented below, we choose the initial position of the geometric center of the flake (located at the middle of the central carbon hexagon) atop one substrate atom and slide it along the armchair direction of the substrate. With this choice, in the moiré reference frame, an observer located at the geometric center of the flake is moving along the x_0 axis with $y_0 = 0$. By substituting this in Eq. (A.2), we then obtain $y'_0 = x'_0 \tan \theta_1$ and $x'_0 = x_0 \cos \theta_1$, which we use for obtaining the dependence of the energy on the position of the flake along the chosen scanline via the integration boundaries in Eq. (A.4).

To calculate the force experienced by the flake at each position, one needs to take a derivative of Eq. (A.4) with respect to the sliding

coordinate, taken to be the armchair direction of the substrate. Notably, sliding one full lattice period along this direction induces a full moiré superlattice period shift along the x axis in the moiré superlattice reference frame (Hermann, 2012; Huang et al., 2022). Hence, taking the derivative of the energy with respect to the sliding direction in the reference frame of the substrate is equivalent to taking the derivative of the energy in the moiré superlattice reference frame with respect to x_0 and correcting for the ratio between the substrate lattice (a_{sub}) and superlattice (a_m) periods:

$$F_{\text{flake}} = \frac{a_m}{a_{\text{sub}}} \left(-\frac{\partial E}{\partial x_0} \right). \quad (\text{A.6})$$

Taking the derivative in Eq. (A.6) using the energy expression of Eq. (A.5) we obtain the following expression for the force experienced by the flake when sliding along the armchair direction of the substrate:

$$\begin{aligned} F_{\text{sqr}}(L, x_0, \theta_1) = & \pm \frac{2\sqrt{3}a_m^2 U_0}{9\pi(1+2\cos 4\theta_1)a_{\text{sub}}} \left[\frac{(1+2\cos 4\theta_1)}{\sin\theta_1 \cos\theta_1} \sin\left(\frac{2\pi L \cos\theta_1}{\sqrt{3}a_m}\right) \sin\left(\frac{4\pi x_0}{\sqrt{3}a_m}\right) \sin\left(\frac{2\pi L \sin\theta_1}{\sqrt{3}a_m}\right) \right. \\ & + 4\sin\left(\frac{2\pi x_0}{\sqrt{3}a_m}\right) \left(\sin\left(\frac{\pi}{3} - 2\theta_1\right) \sin\frac{2\pi L \sin\left(\frac{\pi}{3} - \theta_1\right)}{\sqrt{3}a_m} \sin\frac{2\pi L \cos\left(\frac{\pi}{3} - \theta_1\right)}{\sqrt{3}a_m} \right. \\ & \left. \left. + \sin\left(\frac{\pi}{3} + 2\theta_1\right) \sin\frac{2\pi L \sin\left(\frac{\pi}{3} + \theta_1\right)}{\sqrt{3}a_m} \sin\frac{2\pi L \cos\left(\frac{\pi}{3} + \theta_1\right)}{\sqrt{3}a_m} \right) \right]. \quad (\text{A.7}) \end{aligned}$$

The static friction is defined as the maximum of Eq. (A.7) (after reversing the sign to obtain the force required to initiate motion) along the scanline, $F_s = \max_{\text{scanline}} (-F_{\text{flake}})$. For small θ_1 , the first term in the square parenthesis on the right-hand side of Eq. (A.7), which has a $\sin(\theta_1) \approx \theta_1$ factor in its denominator, dominates, allowing us to neglect the contribution of the second and third terms. With this, the static friction force can be approximated as:

$$F_{\text{s,sqr}}(L, \theta_1) \approx \left| \frac{2\sqrt{3}a_m^2 U_0}{9\pi a_{\text{sub}} \sin\theta_1 \cos\theta_1} \sin\left(\frac{2\pi L \cos\theta_1}{\sqrt{3}a_m}\right) \sin\left(\frac{2\pi L \sin\theta_1}{\sqrt{3}a_m}\right) \right| \approx \left| \frac{2\sqrt{3}a_m^2 U_0}{9\pi a_{\text{sub}} \theta_1} \sin\left(\frac{2\pi L}{\sqrt{3}a_m}\right) \sin\left(\frac{2\pi L \theta_1}{\sqrt{3}a_m}\right) \right|. \quad (\text{A.8})$$

From Eq. (A.8) we see that there are two different periods in the dependence of the static friction on the contact size, a smaller period of $\sim \sqrt{3}a_m/2$ and a larger one of $\sim \sqrt{3}a_m/2\theta_1$. The latter provides the envelope of the static friction force dependence on the contact size:

$$F_{\text{s,sqr}}^{\text{env}}(L, \theta_1) \approx \left| \frac{2\sqrt{3}a_m^2 U_0}{9\pi a_{\text{sub}} \sin\theta_1 \cos\theta_1} \sin\left(\frac{2\pi L \sin\theta_1}{\sqrt{3}a_m}\right) \right|, \quad (\text{A.9})$$

Fig. A3 demonstrates that the approximations taken to obtain Eqs. (A.8) and (A.9), which are used to plot the results presented in Fig. 2c and Fig. 3a, work extremely well for twist angles below 10° and remain valid even for twist angles as large as $\theta = 20^\circ$.

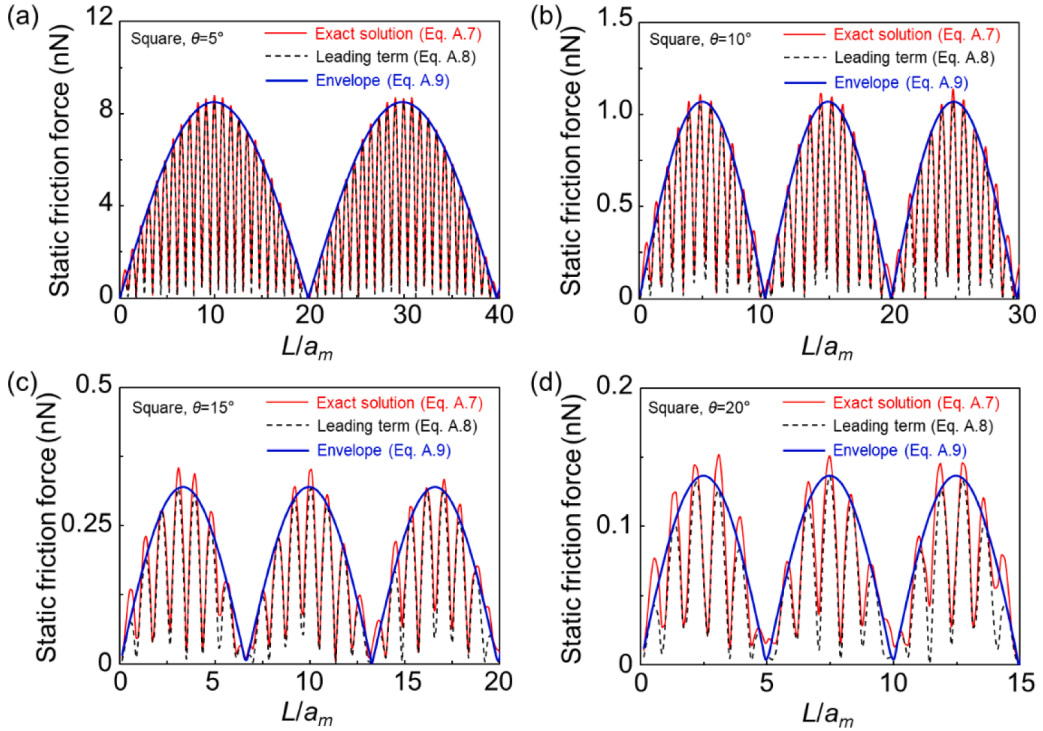


Fig. A3. Comparison of the static friction force dependence on the contact size calculated via the full expression of Eq. (A.7) (black line) and the approximation of Eq. (A.8) (red line) for square graphene flakes sliding on graphene with twist angles of (a) 5°, (b) 10°, (c) 15°, and (d) 20°. The envelopes calculated via Eq. (A.9) are presented by the blue lines.

Finally, we note that in the aligned case ($\theta_1 \rightarrow 0^\circ$), Eq. (A.7) reduces to:

$$F_{\text{sqr}}(L, x_0) = \pm \frac{4a_m^2 U_0}{9\pi a_{\text{sub}}} \left[\frac{\pi L}{a_m} \sin\left(\frac{2\pi L}{\sqrt{3}a_m}\right) \sin\left(\frac{4\pi x_0}{\sqrt{3}a_m}\right) + 2\sin\left(\frac{2\pi x_0}{\sqrt{3}a_m}\right) \sin\left(\frac{\pi L}{a_m}\right) \sin\left(\frac{\pi L}{\sqrt{3}a_m}\right) \right], \quad (\text{A.10})$$

whose maximum as a function of x_0 gives the following for the static friction force:

$$F_{\text{s,sqr}}(L) = \frac{\sqrt{8 - 2c^2 + 2|c|\sqrt{c^2 + 8}} a_m^2 U_0}{9\pi a_{\text{sub}}} \left[2 \left| \sin\left(\frac{\pi L}{\sqrt{3}a_m}\right) \sin\left(\frac{\pi L}{a_m}\right) \right| + \frac{(-|c| + \sqrt{c^2 + 8})\pi L}{2a_m} \left| \sin\left(\frac{2\pi L}{\sqrt{3}a_m}\right) \right| \right], \quad (\text{A.11})$$

where $c = \frac{a_m \sin(\frac{\pi L}{a_m})}{2\pi L \cos(\frac{\pi L}{\sqrt{3}a_m})}$. Note that for large flakes ($L \gg a_m$ and $c \rightarrow 0$) the last term in the square parentheses of Eq. (A.11) dominates yielding the expression for the envelope of the static friction force with flake dimensions, $F_{\text{s,sqr}}^{\text{env}}$, in Eq. (9).

A.2. Circular flakes

For circular shaped flakes, a similar derivation with an appropriate modification of the integration boundaries yields the following expression for the static friction force:

$$F_{\text{s,circ}}(R) = \frac{(3 + \sqrt{33})\sqrt{30 + 2\sqrt{33}}}{72} \frac{a_m \pi R U_0}{a_{\text{sub}}} \left| J_1\left(\frac{4\pi R}{\sqrt{3}a_m}\right) \right|, \quad (\text{A.12})$$

where $J_1(\cdot)$ is the Bessel function of the first kind, and R is the radius of the flake. For large flake radii, the Bessel function can be approximated as (Morovati et al., 2022; Yan et al., 2023):

$$J_1\left(\frac{4\pi R}{\sqrt{3}a_m}\right) \approx \sqrt{\frac{\sqrt{3}a_m}{2\pi^2 R}} \cos\left(\frac{4\pi R}{\sqrt{3}a_m}\right), \quad (\text{A.13})$$

such that Eq. (A.12) yields:

$$F_{s,circ}(R) \approx \frac{(\sqrt{3} + \sqrt{11})\sqrt{5\sqrt{3} + \sqrt{11}}}{24} \frac{a_m^{\frac{3}{2}} R^{\frac{1}{2}} U_0}{a_{sub}} \left| \cos\left(\frac{4\pi R}{\sqrt{3}a_m}\right) \right|, \quad (\text{A.14})$$

which exhibits a single period of $\sqrt{3}a_m/4$ and an upper envelope of:

$$F_{s,circ}^{env}(R) \approx \frac{(\sqrt{3} + \sqrt{11})\sqrt{5\sqrt{3} + \sqrt{11}}}{24} \frac{a_m^{\frac{3}{2}} R^{\frac{1}{2}} U_0}{a_{sub}}, \quad (\text{A.15})$$

with an asymptotic scaling of $R^{\frac{1}{2}}$.

A.3. Triangular flakes

For triangular shaped flakes, a similar derivation with an appropriate modification of the integration boundaries yields the following expression for the force experienced by the flake when sliding along the armchair direction of the substrate:

$$\begin{aligned} F_{tri}(L, x_0, \theta_1) = & \pm \frac{a_m^2 U_0 \cot\theta_1}{3\pi(1 + 2\cos 2\theta_1)a_{sub}} \left[\sqrt{3} \sin \frac{2\pi L \sin\theta_1}{\sqrt{3}a_m} \left(\cos \frac{2\pi(2\sqrt{3}x_0 - L\cos\theta_1)}{3a_m} - \cos \frac{2\pi(\sqrt{3}x_0 + L\cos\theta_1)}{3a_m} \right) \right. \\ & + \tan\theta_1 \left(-\sin \frac{2\pi(\sqrt{3}x_0 - 2L\cos\theta_1)}{3a_m} - \sin \frac{4\pi(\sqrt{3}x_0 + L\cos\theta_1)}{3a_m} \right. \\ & \left. \left. + \cos \frac{2\pi L \sin\theta_1}{\sqrt{3}a_m} \left(\sin \frac{2\pi(\sqrt{3}x_0 + L\cos\theta_1)}{3a_m} + \sin \frac{2\pi(2\sqrt{3}x_0 - L\cos\theta_1)}{3a_m} \right) \right) \right]. \end{aligned} \quad (\text{A.16})$$

A closed form solution for the static friction force is difficult to obtain from Eq. (A.16). Instead, we obtain the static friction force via a numerical search of the maximum force experienced by the triangular flake along the scanline. The envelope of the static friction force dependence on the triangular contact size can be approximated as:

$$F_{s,tri}^{env}(L, \theta_1) \approx \left| \frac{2a_m^2 U_0 \cot\theta_1}{\sqrt{3}\pi(1 + 2\cos 2\theta_1)a_{sub}} \sin \frac{2\pi L \sin\theta_1}{\sqrt{3}a_m} \right|. \quad (\text{A.17})$$

A.4. Hexagonal flakes

For hexagonal shaped flakes, a similar derivation with an appropriate modification of the integration boundaries yields the following expression for the force experienced by the flake when sliding along the armchair direction of the substrate:

$$\begin{aligned} F_{hex}(L, x_0, \theta_1) = & \pm \frac{2a_m^2 U_0}{3\pi(1 + 2\cos 2\theta_1)a_{sub}} \left(\sin \frac{2\pi x_0}{\sqrt{3}a_m} + \sin \frac{4\pi x_0}{\sqrt{3}a_m} \right) \\ & \left(\cos \frac{4\pi L \sin\theta_1}{\sqrt{3}a_m} - \cos \frac{2\pi L \cos\theta_1}{a_m} \cos \frac{2\pi L \sin\theta_1}{\sqrt{3}a_m} + \sqrt{3} \cot\theta_1 \sin \frac{2\pi L \cos\theta_1}{a_m} \sin \frac{2\pi L \sin\theta_1}{\sqrt{3}a_m} \right), \end{aligned} \quad (\text{A.18})$$

from which the following closed form solution for the static friction force can be extracted:

$$F_{s,hex}(L, \theta_1) = \frac{(3 + \sqrt{33})\sqrt{30 + 2\sqrt{33}a_m^2} U_0}{48\pi(1 + 2\cos 2\theta_1)a_{sub}} \left| \cos\left(\frac{4\pi L \sin\theta_1}{\sqrt{3}a_m}\right) - \cos\left(\frac{2\pi L \cos\theta_1}{a_m}\right) \cos\left(\frac{2\pi L \sin\theta_1}{\sqrt{3}a_m}\right) + \sqrt{3} \cot\theta_1 \sin\left(\frac{2\pi L \cos\theta_1}{a_m}\right) \sin\left(\frac{2\pi L \sin\theta_1}{\sqrt{3}a_m}\right) \right|, \quad (\text{A.19})$$

where L is the side length of the hexagonal flake. For small θ_1 , the static friction can be approximated as:

$$F_{s,hex}(L, \theta_1) \approx \frac{(\sqrt{3} + \sqrt{11})\sqrt{30 + 2\sqrt{33}a_m^2} U_0}{16\pi(1 + 2\cos 2\theta_1)a_{sub}} \left| \cot\theta_1 \sin\left(\frac{2\pi L \cos\theta_1}{a_m}\right) \sin\left(\frac{2\pi L \sin\theta_1}{\sqrt{3}a_m}\right) \right|, \quad (\text{A.20})$$

and the envelope is given by:

$$F_{s,hex}^{env}(L, \theta_1) \approx \frac{(\sqrt{3} + \sqrt{11})\sqrt{30 + 2\sqrt{33}a_m^2} U_0}{48\pi(1 + 2\cos 2\theta_1)a_{sub}} \left| \cot\theta_1 \sin\left(\frac{2\pi L \sin\theta_1}{\sqrt{3}a_m}\right) \right|. \quad (\text{A.21})$$

Equations (A.8), (A.14), (A.16) and (A.20) are used to produce the theoretical curves (dashed lines) presented in Fig. 2 and Eqs. (A.9), (A.15), (A.17) and (A.21) are used to trace the envelope curves (blue lines) in Fig. 2 and to derive Eq. (6) of the main text.

At the limit of $\theta_1 \rightarrow 0^\circ$ (the aligned configuration), Eq. (A.19) for the static friction force reduces to:

$$F_{s,\text{hex}}(L) = \frac{(3 + \sqrt{33})\sqrt{30 + 2\sqrt{33}a_m^2}U_0}{72\pi a_{\text{sub}}} \left| \sin^2\left(\frac{\pi L}{a_m}\right) + \frac{\pi L}{a_m} \sin\left(\frac{2\pi L}{a_m}\right) \right|, \quad (\text{A.22})$$

demonstrating asymptotic linear scaling with side length, similar to the square flake case.

References

- Berman, D., Deshmukh, S.A., Sankaranarayanan, S., Erdemir, A., Sumant, A.V., 2015. Macroscale superlubricity enabled by graphene nanoscroll formation. *Science* 348, 1118.
- Cao, W., Hod, O., Urbakh, M., 2022a. Interlayer registry index of layered transition metal dichalcogenides. *J. Phys. Chem. Lett.* 13, 3353–3359.
- Cao, X., Silva, A., Panizon, E., Vanossi, A., Manini, N., Tosatti, E., Bechinger, C., 2022b. Moiré-pattern evolution couples rotational and translational friction at crystalline interfaces. *Phys. Rev. X* 12, 021059.
- Cihan, E., Ipek, S., Durgun, E., Baykara, M.Z., 2016. Structural lubricity under ambient conditions. *Nat. Commun.* 7, 12055.
- Damjanović, M., Vuković, T., Milošević, I., 2002. Super-slippery carbon nanotubes. *Eur. Phys. J. B* 25, 131–134.
- de Wijn, A.S., 2012. (In)commensurability, scaling, and multiplicity of friction in nanocrystals and application to gold nanocrystals on graphite. *Phys. Rev. B* 86, 085429.
- Dienwiebel, M., Verhoeven, G.S., Pradeep, N., Frenken, J.W., Heimberg, J.A., Zandbergen, H.W., 2004. Superlubricity of graphite. *Phys. Rev. Lett.* 92, 126101.
- Dietzel, D., Brndiar, J., Stich, I., Schirmeisen, A., 2017. Limitations of structural superlubricity: chemical bonds versus contact size. *ACS Nano* 11, 7642–7647.
- Dietzel, D., Feldmann, M., Schwarz, U.D., Fuchs, H., Schirmeisen, A., 2013. Scaling laws of structural lubricity. *Phys. Rev. Lett.* 111, 235502.
- Dietzel, D., Ritter, C., Monninghoff, T., Fuchs, H., Schirmeisen, A., Schwarz, U.D., 2008. Frictional duality observed during nanoparticle sliding. *Phys. Rev. Lett.* 101, 125505.
- Dietzel, D., Wijn, A.S.D., Vorholzer, M., Schirmeisen, A., 2018. Friction fluctuations of gold nanoparticles in the superlubric regime. *Nanotechnology* 29, 155702.
- Dong, Y., Vadakkepat, A., Martini, A., 2011. Analytical models for atomic friction. *Tribol. Lett.* 44, 367–386.
- Feng, S., Xu, Z., 2022. Robustness of structural superlubricity beyond rigid models. *Friction* 10, 1382–1392.
- Feng, X., Kwon, S., Park, J.Y., Salmeron, M., 2013. Superlubric sliding of graphene nanoflakes on graphene. *ACS Nano* 7, 1718–1724.
- Filippov, A.E., Dienwiebel, M., Frenken, J.W., Klafter, J., Urbakh, M., 2008. Torque and twist against superlubricity. *Phys. Rev. Lett.* 100, 046102.
- Gigli, L., Manini, N., Benassi, A., Tosatti, E., Vanossi, A., Guerra, R., 2017. Graphene nanoribbons on gold: understanding superlubricity and edge effects. *2D Mater.* 4, 045003.
- Gnecco, E. and Meyer, E. 2007. *Fundamentals of friction and wear*.
- Hartmuth, F., Dietzel, D., de Wijn, A.S., Schirmeisen, A., 2019. Friction vs. area scaling of superlubric NaCl-particles on graphite. *Lubricants* 7, 66–77.
- Hermann, K., 2012. Periodic overlayers and moiré patterns: theoretical studies of geometric properties. *J. Phys.: Condens. Matter* 24, 314210.
- Hod, O., 2010. Quantifying the stacking registry matching in layered materials. *Israel J. Chem.* 50, 506–514.
- Hod, O., 2012. Interlayer commensurability and superlubricity in rigid layered materials. *Phys. Rev. B* 86, 075444.
- Hod, O., Meyer, E., Zheng, Q., Urbakh, M., 2018. Structural superlubricity and ultralow friction across the length scales. *Nature* 563, 485–492.
- Huang, K., Qin, H., Zhang, S., Li, Q., Ouyang, W., Liu, Y., 2022. The origin of Moiré-level stick-slip behavior on graphene/h-BN heterostructures. *Adv. Funct. Mater.* 32, 2204209.
- Kolmogorov, A.N., Crespi, V.H., 2000. Smoothest bearings: interlayer sliding in multiwalled carbon nanotubes. *Phys. Rev. Lett.* 85, 4727–4730.
- Koren, E., Duerig, U., 2016a. Moiré scaling of the sliding force in twisted bilayer graphene. *Phys. Rev. B* 94, 045401.
- Koren, E., Duerig, U., 2016b. Superlubricity in quasicrystalline twisted bilayer graphene. *Phys. Rev. B* 93, 201404 (R).
- Koren, E., Leven, I., Lortscher, E., Knoll, A., Hod, O., Duerig, U., 2016c. Coherent commensurate electronic states at the interface between misoriented graphene layers. *Nat. Nanotechnol.* 11, 752–757.
- Koren, E., Lortscher, E., Rawlings, C., Knoll, A.W., Duerig, U., 2015. Adhesion and friction in mesoscopic graphite contacts. *Science* 348, 679–683.
- Leven, I., Azuri, I., Kronik, L., Hod, O., 2014. Inter-layer potential for hexagonal boron nitride. *J. Chem. Phys.* 140, 104106.
- Leven, I., Guerra, R., Vanossi, A., Tosatti, E., Hod, O., 2016a. Multiwalled nanotube faceting unraveled. *Nat. Nanotechnol.* 11, 1082–1086.
- Leven, I., Krepel, D., Shemesh, O., Hod, O., 2013. Robust superlubricity in graphene/h-BN heterojunctions. *J. Phys. Chem. Lett.* 4, 115–120.
- Leven, I., Maaravi, T., Azuri, I., Kronik, L., Hod, O., 2016b. Interlayer potential for graphene/h-BN heterostructures. *J. Chem. Theory Comput.* 12, 2896–2905.
- Liao, M., Nicolini, P., Du, L., Yuan, J., Wang, S., Yu, H., Tang, J., Cheng, P., Watanabe, K., Taniguchi, T., Gu, L., Claerbout, V.E.P., Silva, A., Kramer, D., Polcar, T., Yang, R., Shi, D., Zhang, G., 2021. Ultra-low friction and edge-pinning effect in large-lattice-mismatch van der Waals heterostructures. *Nat. Mater.* 21, 47–53.
- Liu, Z., Yang, J., Grey, F., Liu, J.Z., Liu, Y., Wang, Y., Yang, Y., Cheng, Y., Zheng, Q., 2012. Observation of microscale superlubricity in graphite. *Phys. Rev. Lett.* 108, 205503.
- Lozovik, Y.E., Minogin, A.V., Popov, A.M., 2003. Nanomachines based on carbon nanotubes. *Phys. Lett. A* 313, 112–121.
- Maaravi, T., Leven, I., Azuri, I., Kronik, L., Hod, O., 2017. Interlayer potential for homogeneous graphene and hexagonal boron nitride systems: reparametrization for many-body dispersion effects. *J. Phys. Chem. C* 121, 22826–22835.
- Mandelli, D., Guerra, R., Ouyang, W., Urbakh, M., Vanossi, A., 2018. Static friction boost in edge-driven incommensurate contacts. *Phys. Rev. Mater.* 2, 046001.
- Morovati, V., Xue, Z., Liechti, K.M., Huang, R., 2022. Interlayer coupling and strain localization in small-twist-angle graphene flakes. *Extreme Mech. Lett.* 55, 101829.
- Müser, M.H., 2004. Structural lubricity: role of dimension and symmetry. *Europhys. Lett.* 66, 97.
- Müser, M.H., Wenning, L., Robbins, M.O., 2001. Simple microscopic theory of Amontons's laws for static friction. *Phys. Rev. Lett.* 86, 1295–1298.
- Ouyang, W., Mandelli, D., Urbakh, M., Hod, O., 2018. Nanoserpents: graphene nanoribbons motion on two-dimensional hexagonal materials. *Nano Lett.* 18, 6009.
- Özoğul, A., Ipek, S., Durgun, E., Baykara, M.Z., 2017. Structural superlubricity of platinum on graphite under ambient conditions: the effects of chemistry and geometry. *Appl. Phys. Lett.* 111, 211602.
- Qu, C., Wang, K., Wang, J., Gongyang, Y., Carpick, R.W., Urbakh, M., Zheng, Q., 2020. Origin of friction in superlubric graphite contacts. *Phys. Rev. Lett.* 125, 126102.
- Sharp, T.A., Pastewka, L., Robbins, M.O., 2016. Elasticity limits structural superlubricity in large contacts. *Phys. Rev. B* 93, 121402 (R).
- Song, Y., Mandelli, D., Hod, O., Urbakh, M., Ma, M., Zheng, Q., 2018. Robust microscale superlubricity in graphite/hexagonal boron nitride layered heterojunctions. *Nat. Mater.* 17, 894–899.
- Steiner, P., Roth, R., Gnecco, E., Baratoff, A., Maier, S., Glatzel, T., Meyer, E., 2009. Two-dimensional simulation of superlubricity on NaCl and highly oriented pyrolytic graphite. *Phys. Rev. B* 79.
- Vanossi, A., Bechinger, C., Urbakh, M., 2020. Structural lubricity in soft and hard matter systems. *Nat. Commun.* 11, 4657.
- Varini, N., Vanossi, A., Guerra, R., Mandelli, D., Capozza, R., Tosatti, E., 2015. Static friction scaling of physisorbed islands: the key is in the edge. *Nanoscale* 7, 2093–2101.
- Verhoeven, G.S., Dienwiebel, M., Frenken, J.W.M., 2004. Model calculations of superlubricity of graphite. *Phys. Rev. B* 70, 165418.
- Wang, J., Cao, W., Song, Y., Qu, C., Zheng, Q., Ma, M., 2019a. Generalized scaling law of structural superlubricity. *Nano Lett.* 19, 7735–7741.
- Wang, K., Ouyang, W., Cao, W., Ma, M., Zheng, Q., 2019b. Robust superlubricity by strain engineering. *Nanoscale* 11, 2186–2193.
- Wang, K., Qu, C., Wang, J., Ouyang, W., Ma, M., Zheng, Q., 2019c. Strain engineering modulates graphene interlayer friction by moiré pattern evolution. *ACS Appl. Mater. Interfaces* 11, 36169–36176.

- Yan, W., Ouyang, W., Liu, Z., 2023. Origin of frictional scaling law in circular twist layered interfaces: simulations and theory. *J. Mech. Phys. Solids* 170, 105114.
- Yan, W., Shui, L., Ouyang, W., Liu, Z., 2022. Thermodynamic model of twisted bilayer graphene: entropy matters. *J. Mech. Phys. Solids* 167, 104972.
- Yaniv, R., Koren, E., 2019. Robust superlubricity of gold–graphite heterointerfaces. *Adv. Funct. Mater.* 30.